Ultra-wideband 3D-printed vivaldi array for in-band full-duplex applications with a grating lobes reduction approach

Hadi Hijazi, Marc Le Roy, Raafat Lababidi, Denis Le Jeune, Andre Pérennec

Contents lists available at ScienceDirect

International Journal of Electronics and Communications

https://www.sciencedirect.com/journal/aeu-international-journal-of-electronics-and-communications

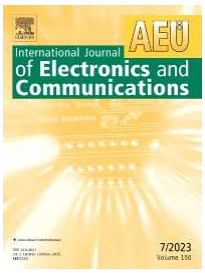

Ultra-Wideband 3D-Printed Vivaldi Array for In-Band Full-Duplex Applications with a Grating Lobes Reduction Approach

Hadi Hijazi[a,b]*, Marc Le Roy[b], Raafat Lababidi[a], Denis Le Jeune[a], Andre Pérennec[b]

[a] *ENSTA Bretagne and* [b]*Univ Brest, Lab-STICC, CNRS, UMR 6285, F-29200 Brest, France*
**hadi.hijazi@ensta-bretagne.org*

Abstract

This work validates the ability for in-band full-duplex systems to operate over ultra-wide bandwidths. As a proof of concept an ultra-wideband in-band full-duplex antenna array was designed. The array is formed of two wideband microstrip-slotline baluns and four Vivaldi antennas in a 3D-printed single-piece structure. The metal thickness of the 3D-printed Vivaldi antennas makes them sturdier than PCB antennas and more immune to fracturing or breaking, however, they require a coax-to-slot transition as a feeding mechanism. Such transitions are not well documented in the literature, specifically, the effect of metal thickness on the impedance of the 3D-printed slotline. Therefore, impedance curves for the 3D slot are provided as a function of its width and metal thickness. Then, a prototype was realized and measured, it achieves about 40 to 80 dB of self-interference cancellation (SIC) in the frequency range from 4.4 GHz to 28.7 GHz for an average gain of 9.8 dBi with a directive end-fire radiation pattern. The only drawback of this first prototype is the presence of grating lobes in its radiation pattern due to the separation distance between the opposite antennas which exceeds a half-wavelength. Despites the antenna placement requirement in order to achieve near-field self-interference cancellation, , we manage to mitigate those grating lobes by using an approach based on a partial size reduction at the bottom of the antenna. This allows bringing the antennas closer together at their bottom parts, reducing the distance between the radiating slots, which translates to grating lobes reduction especially at higher frequencies. The implementation of this approach results in keeping all sidelobes 10 dB below the main lobe level while keeping the FoM of this 2nd UWB IBFD antenna system at a higher level compared to existing techniques.

Keywords: 3D-printing; grating lobes reduction; in-band full-duplex; self-interference cancellation; ultra-wideband; Vivaldi antenna.

1. Introduction

The ability for radios to simultaneously transmit and receive (STAR) using the same frequency band has become possible with the advent of in-band full-duplex (IBFD) technology. This ability was hindered by the high self-interference (SI), or the direct power coupling, between the receiver of a radio and its own transmitter. However, IBFD manages to establish a STAR wireless communication by employing various methods to suppress SI to below the receiver's noise floor, such that it does not significantly impact the receiver's signal-to-noise ratio [1]. Following that, at least 110 dB of Self-Interference Cancellation (SIC) are required to establish an IBFD communication [2], and those can be accumulated at the different levels of the radio front-end: at the antenna, analog, and digital levels. But most importantly, it is critical to achieve a notable amount of SIC at the antenna level (or at least at the RF stage) to avoid saturating the receiver or degrading its quantization resolution. Therefore, our work only focuses on antenna-level SIC techniques.

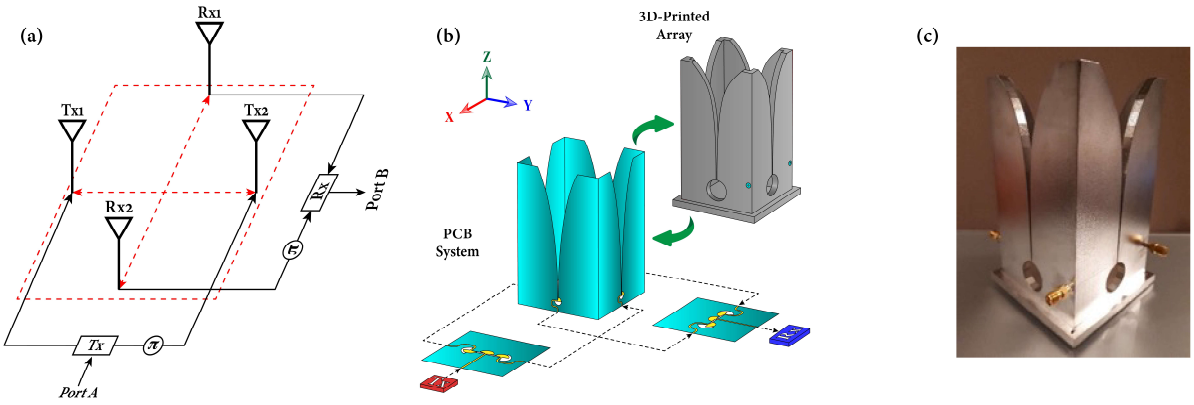

Figure 1: (a) system configuration, (b) an illustrative drawing of the PCB system with the 3D-printed Vivaldi array in the background, and (c) a picture of the fabricated 3D-printed Vivaldi array.

Previously, numerous techniques were proposed in the literature to obtain high levels of SIC at the antenna level. The reader can refer to [3] for an exhaustive review. However, most of the presented techniques were mainly narrowband. Yet, it would be more desirable to implement a wideband IBFD antenna system that can be used as multi-standard radio for applications requiring high data-rate links or frequency reconfigurability, like radars, cognitive radios, or base stations. Unluckily, the subject of wideband IBFD systems was not widely explored in the literature so more effort needs to be invested in that field. Among the few works on that topic, the team at Colorado University have implemented multiple antenna systems [4-6] to cover the frequency range from 0.5 to 40 GHz, but their system is bulky and expensive. So, it would be more convenient to have a compact and low-cost single system that can serve multiple bands and standards.

Based on the above, in a previous work, we have designed an ultra-wideband IBFD antenna system that spans the frequency range from 4-40 GHz with at least 50 dB of self-interference cancellation [7]. The proposed system was configured as in Fig. 1, and it is composed of a 4-element PCB Vivaldi array and two baluns based on microstrip-slotline transitions. The wideband performance of both the antennas and baluns can be attributed to the wideband behavior of the microstrip-slotline transitions used in both devices. And those transitions were optimized for maximum bandwidth based on a previous study [8]. The four Vivaldi antennas in the array are placed vertically toward the direction of radiation, and then sequentially rotated around the center of the array as shown in Fig. 1(b). Thus, they form two pairs of orthogonally polarized antennas: one pair will be used to transmit while the other will be used to receive. Such antenna configuration is mandatory for proper system radiation and SIC. Each antenna pair was then connected to an external balun that delivers, to the opposite antennas, two signals of equal amplitudes and inverted phases. The two radiated waves from the opposite antennas will cancel each other in the near-field region (as demonstrated in [3]) where the other pair exists, and, at the same time, they will recombine constructively in the far-field region. The near-field cancellation and the orthogonal polarizations will ensure that the self-interference signals radiated by the transmit antennas will be cancelled by a significant amount (> 50 dB) before reaching the receive antennas.

But despite its wideband performance, the fabricated system suffered from three major drawbacks:

(i) Gain degradation due to high substrate losses: In fact, all system components were built on a Rogers RO4003C substrate (ε_r = 3.55, tanδ = 0.0027) which proved to be very lossy in practice, especially at higher frequencies, leading to a significant drop in gain. Therefore, it is favorable to replace it with another substrate having lower loss tangent; like Rogers RT5880 (ε_r = 2.2, tanδ = 9×10^{-4}); or remove the substrate all together.

(ii) Mechanical fragility due to low substrate thickness and the need for external support to hold the antennas: The wideband behavior of the microstrip-slotline transitions heavily relied on using a substrate with very low thickness ($h = 203.2\ \mu m$), but this came at the expense of system's fragility and the need for an auxiliary support to hold the antennas and protect them from external forces. To overcome this, the thickness of the substrate can be increased but a portion of the bandwidth must be sacrificed.

(iii) Presence of grating lobes in the radiation patterns, especially at higher frequencies, due to excessive antenna separation in comparison to the corresponding wavelength. Those grating lobes emerge when the separation

distance between the two opposite antennas is higher than a half-wavelength at the corresponding frequency. This means that the grating lobes will be more significant at higher frequencies, and will multiply in number, considering that the separation distance will be higher than a multiple of half-wavelength. Therefore, system size must be modified to reduce the grating lobes effect.

The mechanical drawbacks compel us to increase the thickness of our components to avoid damaging them, however, this comes at the expense of losing a portion of the wide bandwidth. Moreover, even if a thicker substrate is used, there is still a need for an external support to hold and align the antennas. In addition to that, we have envisaged a way to mitigate grating lobes that requires modifying the shape and profile of the antenna, but PCB technology is not compatible with such modifications. Therefore, we saw that it would be better to transition from PCB technology to 3D-printing to build our Vivaldi array, as shown in Fig. 1(b). Since with PCB antennas, there are only few degrees of freedom that can be manipulated to enhance their performance, while with 3D-printed antennas, one can freely manipulate antenna's shape and metal thickness to modify system's behavior. And most importantly, the array can be built in a single piece with all the antennas aligned properly and without the need for an auxiliary support.

Thus, in this article, two 3D-printed IBFD UWB antenna systems are presented: System I is an evolution of the PCB Vivaldi array to a 3D-printed array, and this evolution will be explained in detail in the next section along with a demonstration of a fabricated prototype and its mechanical and electrical performances. The third section will present a modified system, System II, which implements a new approach to mitigate grating lobes based on manipulating antenna's shape and size. Finally, the last section will conclude and point to future perspectives.

1. System I: Evolution from PCB to 3D-Printing

1.1. Array Design:

3D-printed Vivaldi antennas exhibit several advantages over PCB antennas: (i) they can be built as one piece without the need for external support, and, therefore, they can be sturdier and can endure harsh environments. (ii) They can have higher power handling capability. (iii) They exhibit thicknesses significantly higher than that of PCBs (few millimeters for 3D-printed antennas vs. few micrometers for PCB antennas). Thus, they will incur less resistive losses since the currents flowing on the antennas' flares will be spread over a wider area than that of PCB antennas. This will reduce the surface current density and consequently will reduce the resistive losses [9]. (iv) They are built without a dielectric substrate and are only surrounded by air, which eliminates the majority of dielectric losses, if not all.

Like PCB Vivaldi antennas, which are usually fed by a microstrip-to-slotline transition, 3D-printed Vivaldi antennas are fed by a coax-to-slot transition (also called coax-to-ridge transition), as depicted in Figure 2(b). In this context, we mean by slot the space or separation between the opposite flares of the antenna. And the feeding transition must take into account the effect of metal thickness (T) on system matching. But since the slot is only surrounded by air and uses no substrate, then, the two factors that determine its impedance are its width (W_s) and metal thickness (T). However, in the literature, there are no closed-form equations that describe the variation of the slot impedance as a function of its width and thickness, thus we studied this variation empirically by means of full-wave simulations.

The results of the full-wave simulations are depicted in Figure 2(c), and they indicate that the impedance of the slot increases if the slot width (W_s) is increased or if the metal thickness (T) is decreased. Also, a slight change in the slot width has a major impact on its impedance whereas a change in the metal thickness has less impact. Moreover, multiple values of slot width and metal thickness can yield the same impedance, thus before choosing the dimensions of the slot, which will determine its impedance, several factors must be taken into consideration:

- If a coaxial line with 50 Ω is to be used to feed the antenna, then the impedance of the slot needs to be designed to match the impedance of the coaxial feed.
- The antennas need to be thick enough to endure external pressure and not break easily or bend. So, according to our experience, a thickness of 5 mm can be sufficient.
- Also, the thickness of the antennas needs to be greater than the outer diameter of the coaxial feed ($T > D_o$), which will be embedded inside the body of the antenna.

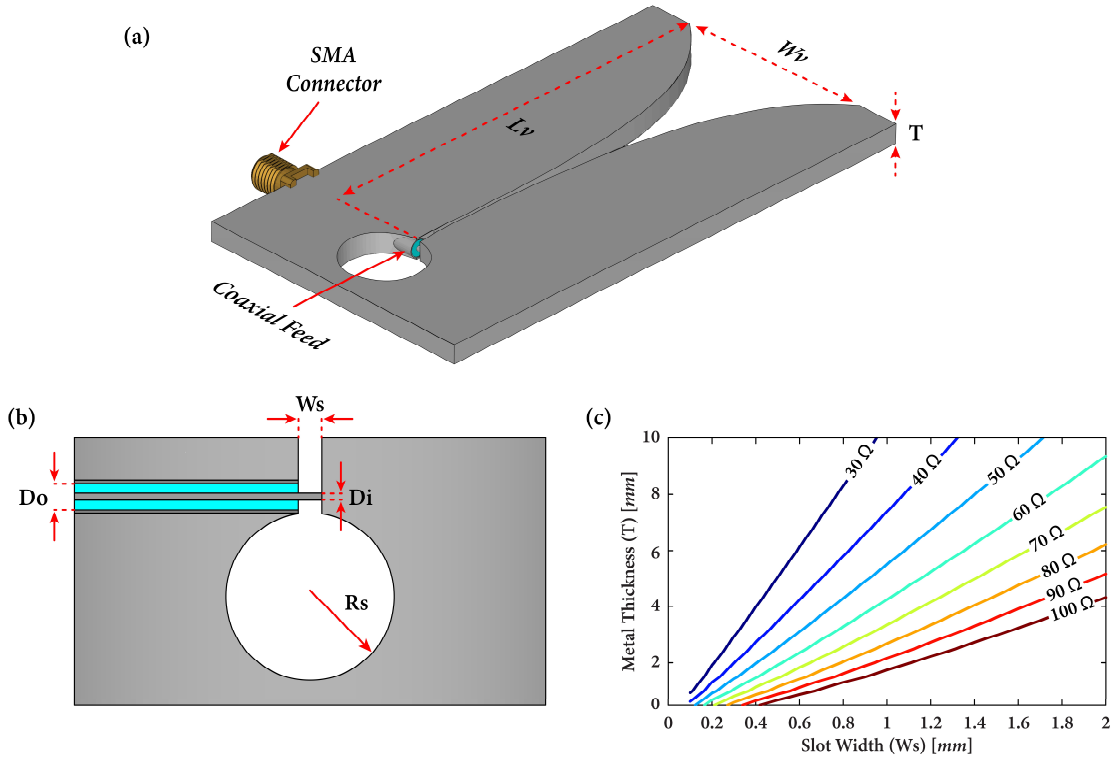

Figure 2: (a) an illustrative drawing of a 3D-printed Vivaldi antenna, (b) a side view of the coax-to-slot transition, and (c) 3D slot impedance as a function of its width and thickness. {T = 5.6 *mm;* Wv = 50 *mm* ; Lv = 100 *mm*; Ws = 1 *mm*; Rs = 10 *mm*; Do = 3.58 *mm*; Di = 0.92 *mm*}

- As the minimum slot width determines the highest frequency that can be radiated by the antenna, the narrowness of the slot width (W_s) while maintaining a relatively high metal thickness (T) will be particularly critical in 3-printing technology .

From those specifications, the different slot widths and metal thicknesses corresponding to a 50 Ω slot were extracted by simulation, and their values are plotted in the graph of Figure 2(c). We chose the slot width (W_s) to be 1 mm in order to remain within the limits of the 3D-printing process, and the corresponding metal thickness (T) was found to be 5.6 mm. The chosen slot width limits the highest frequency of operation to around 25 GHz (based on simulations), nonetheless, the obtained bandwidth is still very wide and can cover multi-standard applications.

In addition to the above, the coaxial feed line must have an outer diameter that is sufficiently less than the thickness of the metal (D_o < T). And there are several commercially available coaxial cables that can satisfy this requirement. But there is another condition that also needs to be satisfied for optimum matching. In fact, simulations revealed that, for better matching between the coax and the slot, the difference between the outer radius and the inner radius of the coaxial line must be exactly equal to the slot width ($[D_o - D_i] / 2 = W_s$), otherwise the matching is degraded. Commercially available coaxial lines come in preset dimensions, and the ones that can almost satisfy the requirements are 0.141-inch cables (D_o = 3.58 mm).

After satisfying the impedance matching conditions between the coaxial line and the slot, a slot stub is needed to transition smoothly from coax to slot and to ensure proper matching. Here a circular stub was used, and its radius (R_s) determines the lowest frequency of matching, while the length of the exponential taper (L_v) and the width of the aperture (W_v) determines the lowest frequency of radiation. The radius of the stub was initially set to 10 mm, and it provides a matching bandwidth down to 2 GHz (based on simulations). Now, if the antenna is required to radiate properly at 2 GHz, then the length of the exponential taper (L_v) must be one wavelength (λ = 150 mm) and the width of the aperture (W_v) must be about a half wavelength [10], which means that the size of the antenna will be relatively big. In fact, the 3D-printer has a limit on the size of the printed objects, such that big objects, which might exceed the

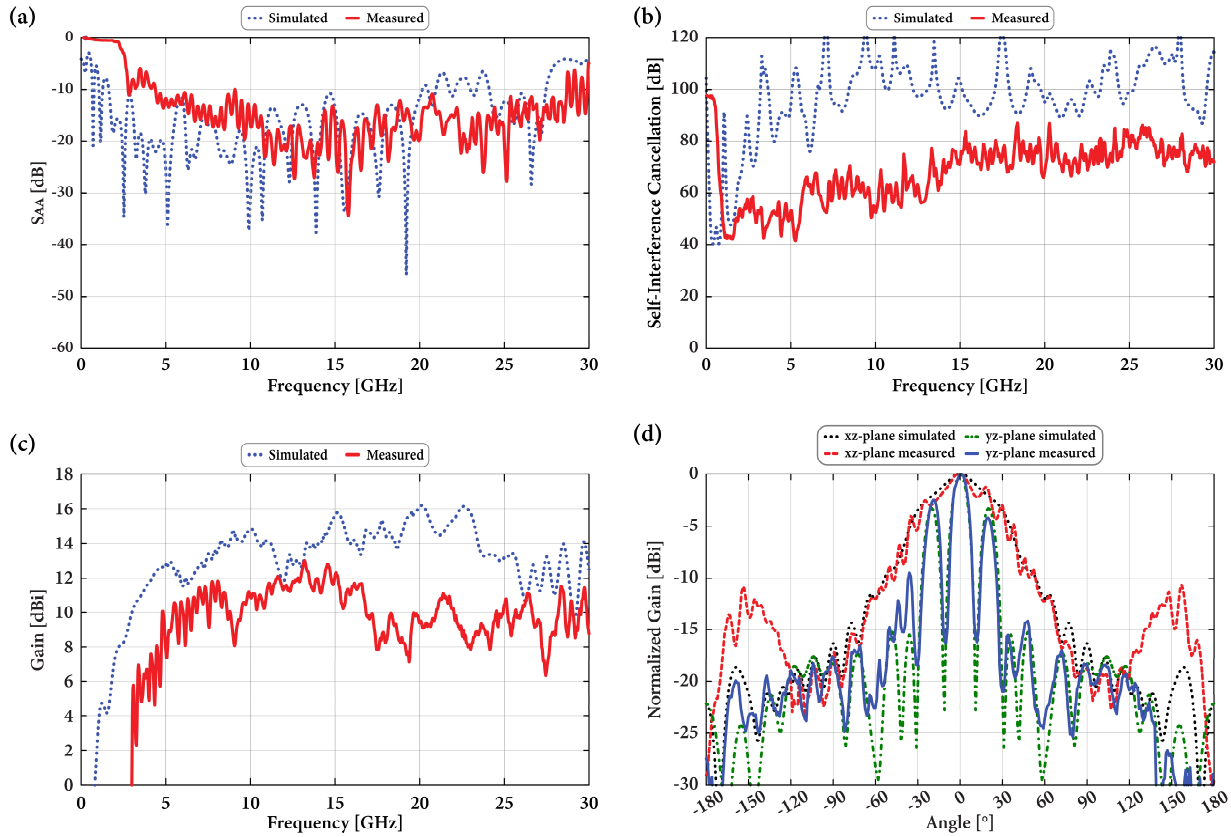

Figure 3: simulated and measured (a) system matching, (b) self-interference cancellation, (c) broadside gain, and (d) radiation pattern at 10 GHz.

size limit, need to be printed in several parts and then assembled after. For us, it was more important to print the antennas as one piece to ensure that they will be sufficiently robust and solid. Thus, to be consistent with the 3D-printer limitations, the length of the exponential taper (L_v) was decreased to one wavelength at 3 GHz (λ = 100 mm).

Based on the above analysis a 3D-printed Vivaldi array was simulated and fabricated, and it is shown in Fig. 1(c). The fabricated prototype was 3D-printed using a Clear V4 epoxy resin (with ε_r = 2.87 and tanδ = 0.0027), and then sandblasted to enhance its surface roughness.Thus, the antenna system was metalized following a 3-step process: a 3 µm chemical copper deposition preceded by palladium catalysis, a 10 µm electrolytic copper deposition, and a 10 µm electrolytic tin deposition which gives the antennas their silver color. Finally, note that although 3D-printed antennas are sturdier than PCB antennas, yet multiple mechanical defects might be present in the 3D-printed prototype:

- The 3D-printing process has its own tolerances, so the spacing between the flares of the antenna (the slot width) might not have the same exact value as in the simulated model.
- After the 3D printer finishes printing the antenna, it is immersed in a hot liquid metal bath to perform the chemical copper deposition. The heat exposure from the metal bath manages to deform the antenna, and the misalignment between its flares becomes more significant.
- Although the 3D-printed antennas are more solid and rigid than the PCB ones, but, after all, if a sufficient force is applied to it, for example, if the antenna is squeezed forcefully by hand, the antenna flares can bend or move closer to one another.

The misalignment and the change in the separation between the flares can cause the slot impedance to change, which means that it would not be surprising to observe some impedance mismatches in measurement.

1.2. System Performance

To finalize the system, two wideband baluns based on microstrip-to-slotline transitions were designed following our work in [8], but they were modified to operate in the same frequency range of the antennas (2-20 GHz). The performance of the baluns is not demonstrated here for brevity, but the readers are advised to explore [8] for additional information. Measurements were conducted after connecting the baluns to the antennas using four Keysight N5448B phase-paired cables, while simulations were performed separately for the baluns, cables, and antennas, and then their S-parameters were combined numerically. The simulated and measured results are depicted in Figure 3.

The simulated matching bandwidth in Fig. 3(a) starts at 3 GHz and ends at 19.5 GHz with some spikes in the curve that almost reach -10 dB. On the other hand, the measured matching bandwidth spans the frequency range from 4.4 GHz to 28.65 GHz where the matching level seems to be better than simulation. The better matching in measurements seems to be related to the higher losses of the used devices (baluns, cables, connectors...) which reflect positively on the measured return loss. Figure 3(b) also reveals that the simulated SIC level remains above 60 dB throughout the bandwidth with an average value of 90 dB, except for some spikes at some frequencies. On the other hand, the measured SIC remains higher than 40 dB at the low frequency side and reaches 80 dB at the high frequency side. Note that, it is normal to have differences between the simulated and measured SIC levels for two reasons: (i) the simulated balun has less phase and amplitude imbalances than the measured one, and (ii) the imperfections in the 3D-printing process affect the symmetry of the array leading to a slight misalignment between the different elements of the array. Both the imbalances and the asymmetry can lead to a significant degradation in the SIC performance.

Moreover, the simulated system gain in Figure 3(c) gets higher than 10 dBi starting from 3 GHz and maintains an average value of 12.5 dBi, while the measured gain reaches 5 dBi at 3 GHz and maintains an average value of 9.8 dBi, then it starts dropping again around 18 GHz. Of course, the measured gain was expected to be lower than the simulated one due to the high losses in the fabricated baluns, but also this might be caused by some frequency limitations of the measurement equipment used in the anechoic chamber. Finally, Figure 3(d) depicts sample radiation pattern cuts at 10 GHz, and it seems that there is a good agreement between simulations and measurements in general. In the xz-plane, a main lobe and two grating lobes are observed, while all other side lobes are at least 10 dB below the main lobe level. The presence of the grating lobes is related to the fact that the separation between the opposite antennas is higher than a half wavelength at the measured frequency, and their presence is common in Vivaldi arrays [7, 11]. On the other hand, in the yz-plane, the simulated and measured main lobes are highly similar, but there is a slight difference in the side lobes level. It seems that the fabricated antenna has two significant back lobes, which are 10 dB below the main lobe level, but remain much higher than from simulation. It is surprising to have back lobes in measurements especially that the square base at the bottom of the array should, normally, force the energy to radiate to the front. It seems that some of the currents flowing on the surface of the array manage to reach the reflector, and the reflector in turn radiates those currents from its edges.

Finally, in our previous work [7], we proposed a new figure of merit ($\mathrm{FoM_{WFD}}$) in order to compare performance of wideband in-band full-duplex antenna systems. $\mathrm{FoM_{WFD}}$ takes into account the system's bandwidth, gain, size, and level of self-interference cancellation. The measured 3D-printed system here scores 7.34 on the proposed figure of merit while the PCB system in our previous work had scored 6.66[†]. So, in summary, the 3D-printed array managed to circumvent several mechanical defects present in the PCB system and enhance the gain, thus, making our current system sturdier and more efficient. This came at the expense of a reduced matching bandwidth. But despite that, the 3D-printed system achieved a higher score on $\mathrm{FoM_{WFD}}$ than the PCB one and than other references on UWB IBFD antenna systems, which means that overall, not only the mechanical problems were fixed but also the in-band full-duplex performance of the system was enhanced in its corresponding bandwidth.

[†] These values were obtained by using a corrected calculus slightly different than the one used in [7].

2. System II: Grating Lobes Reduction

2.1. Array Design:

Based on the fact that grating lobes originate from the excessive separation distance between the radiating antennas, particularly as it becomes greater than a half-wavelength, the obvious solution would be to bring the antennas closer together. However, since the antennas are configured in a box-like configuration where the transmit antennas are placed in-between the receive antennas, and vice versa, then the separation distance between one pair of antennas will be defined by the width of the other pair of orthogonal antennas. But since all antennas are identical, then the separation distance between the opposite antennas is conditioned by the width of the single element, which is higher than λ/2 at the lowest frequency to ensure proper matching and radiation at the low-frequency end of the bandwidth.

Shrinking the size of the antenna will lead to a reduction in its electrical length, and this in turn will lead to system performance deterioration at those low frequencies, which is undesirable in this case. The reduced width can be compensated for by creating some corrugations in the sides of the antennas, which increases its electrical perimeter while keeping its size fixed. This permits the nonradiated surface currents to dissipate in the corrugations preventing them from reflecting to the input port. While this approach can preserve system matching, it cannot prevent the deterioration in its radiation at low frequencies. On the contrary, it might cause the corrugations to radiate to the sides of the antenna raising the levels of sidelobes.

Alternatively, an approach based on a partial width reduction can be considered a more acceptable solution. The rationale for this approach is based on three premises: (i) the grating lobes are much significant at higher frequencies where the separation distance becomes higher than multiples of a half-wavelength, (ii) the high-frequency radiation is emitted from the lower parts of the exponentially tapered slot while the low-frequency radiation is emitted from the upper parts of the slot, and (iii) the top part width is necessary for proper low-frequency radiation while the bottom part width is not critical for high-frequency radiation.

Then, it can be inferred that by reducing the width of the bottom part (W_b) of the single antenna, while keeping the same top part width (W_t), the radiation performance of the single element shall not be affected. This permits to bring the four antennas in the array closer together at their bottom parts, as shown in Fig. 4(a), while preserving the same separation at their top parts. Thus, in this case, the outer body of the single antenna element is linearly tapered, and it would be necessary to tilt the antennas in the array to form an inverted-pyramid-like shape. And the tilt angle (θ) with respect to the z-axis is given by:

$$\theta = sin^{-1}\left(\frac{W_t - W_b}{2L_v}\right) \qquad (1)$$

where W_t and W_b are the widths of the top and bottom parts of the antenna, respectively, and L_v is the length of the radiating slot. It follows that the bottom parts of the slots, which are responsible for high-frequency radiation, are now closer than before, and this should mitigate the grating lobes at higher frequencies. But on the other hand, the low-frequency radiation will be insignificantly affected by this approach.

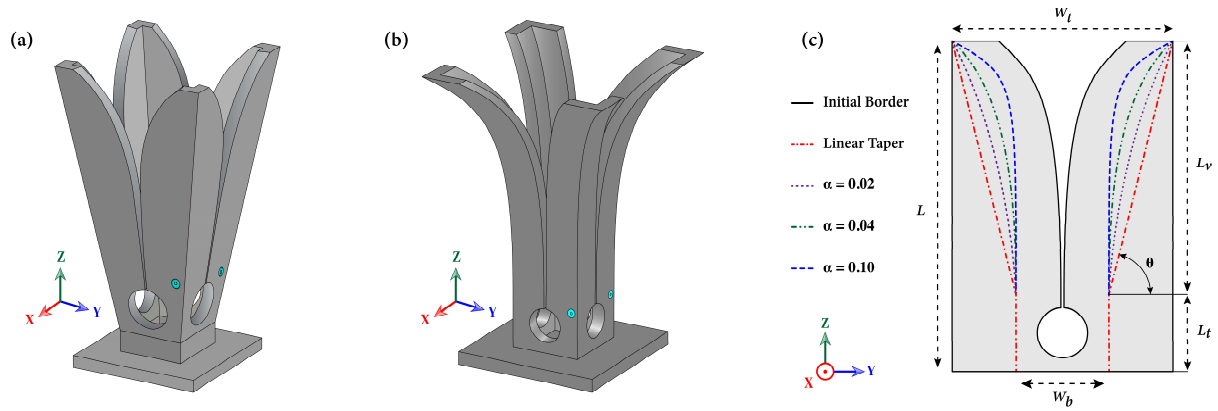

Figure 4: (a) a 3D-printed Vivaldi antenna with different outer body tapers and modified Vivaldi arrays with (b) linearly tapered outer body and (c) exponentially tapered outer body. {Wt = 75 *mm*; Wb = 25 *mm*; Lv = 100 *mm*; Lt = 30 *mm*; L = 130 *mm*}

This approach can be pushed forward further by exponentially tapering the outer body of the antenna as in Fig. 4(b), giving the array a lily-flower-like shape. Exponential tapering of the antennas' bodies allows the lower and central parts of the antennas to be brought even closer towards the center of the array, as opposed to the fixed separation provided by the linear taper. To better visualize this, take a look at Fig. 4(c) and consider that the exponential taper of the outer body of the antenna is defined by the following equations:

$$y = Ae^{\alpha x} + B \tag{2}$$

$$A = \frac{0.5(W_t - W_b)}{e^{\alpha L} - e^{\alpha L_t}} \tag{3}$$

$$B = \frac{0.5(W_b e^{\alpha L} - W_t e^{\alpha L_t})}{e^{\alpha L} - e^{\alpha L_t}} \tag{4}$$

where L is the total length of the antenna, L_t is the length of the part containing the coax-to-slot transition, and α is the exponential growth rate. It is obvious from Fig. 4(c) how the outer border of the antenna is moving inward as the exponential growth rate (α) is increased. The more α is increased, the more the central parts of the antennas will move inward, bringing the opposite radiating slots even closer to one another, which boosts the mitigation of grating lobes as compared to the level of grating lobes reduction provided by the linear taper.

However, this approach cannot be exploited indiscriminately, the value of α should be chosen carefully as a compromise between different system parameters. In this case α was set to 0.05. Finally, note that although this approach alone is not sufficient to eliminate grating lobes entirely, it remains a better arrangement than the initial design. Nevertheless, there should be a concern whether the tilt in the antennas would cause some problems in the array's performance, considering that the radiation of the single element is not emitted along the broadside direction, but rather along a slightly tilted path. This issue will be discussed and analyzed next.

2.2. Simulation Results:

Simulations were carried out using CST Microwave Studio in which the antennas were modeled as perfect electric conductors (PECs). Equally, the metallic parts of the coaxial cables were also modeled as PECs, while the dielectric part of the coax was modeled as Teflon (ε_r = 2.1, tanδ = 2×10^{-4}). Moreover, two microstrip-slotline baluns operating in the frequency range from 2 to 20 GHz were also designed and simulated based on [6]. The results of the simulation are depicted in Fig. 2, and they compare two different systems: 'System I' is the 3D-printed design from the previous section as in Fig. 1, where the antenna size is uniform and there is no size reduction. And 'System II' is the 3D-printed lily-shaped design in Fig. 4(b) where the antenna size is reduced at the bottom and its body is exponentially tapered.

Beginning with system matching in Fig. 5(a), it seems that both systems exhibit similar matching figures, where both systems are well matched over a decade bandwidth from 2 to 20 GHz. Equally, it can be said that both systems exhibit similar self-interference cancellation performance, where in Fig 4(b), the level of cancellation remains higher

than 60 dB and it maintains an average value of 100 dB. Note that these values are idealistic and are expected to be lower in practice, since they ignore the impact of fabrication intolerances, and the imbalances between the balun's outputs on the array's performance. In addition to the above, Fig. 4(c), 4(d), and 4(e) depict some radiation pattern plots at 10, 15, and 20 GHz, respectively. The plotted radiation patterns indicate that the yz-plane cuts are quite similar for both systems, though it can be said, in general, that System II exhibits lower sidelobe levels. Also, it is evident that grating lobes are only present in thexz-plane, and that their levels are much lower for System II. Moreover, other sidelobes in general are lower in System II. In fact, the obtained grating lobe reduction is about 9.5, 8.7, and 7.4 dB at 10, 15, and 20 GHz, respectively. And this confirms the validity of the grating lobe reduction approach proposed here. At last, those figures show that the radiation at all frequencies is directed along the broadside, which means that tilting the antennas does not cause a tilt in the direction of the array's radiation.

Finally, the gain plots in Fig. 2(f) show that the average gain of System I in the matching bandwidth is about 13.2 dBi, while it is 12.8 dBi for System II. For both plots, there are some gain dips at some frequencies; for example, around 6~7 GHz; however, they seem stronger for System II and occurring at slightly different frequencies. Our simulations revealed that, for both systems, there is a strong direct coupling between the opposite antennas at those frequencies. This direct coupling does not hinder the self-interference cancellation performance of the system, but it surely degrades its gain. And although we were not able to exactly pinpoint the root cause of this problem, yet our simulations indicate that at some point along the radiating slot, the surface currents traveling along the antenna flares are being jammed and concentrated at that point, then the concentrated currents couple to the opposite antenna. We think that this issue is caused by the exponential shape of the antenna, and by simply manipulating its profile we observe changes in its gain and the concentration of surface currents at that point. In addition to that, there is a high correlation between this phenomenon and the size of the matching stubs and the proximity of the two opposite stubs. More precisely, if the size of the stub is reduced, or if the separation between the opposite stubs is increased, then the gain dips become less significant or occur outside the matching bandwidth. However, any further modifications to reduce gain dips, whether by changing antennas' shape or the separation between them, will have a negative impact on grating lobes reduction or self-interference cancellation. Hence, we believe that the current configuration is a good compromise between all, and one can find a useful bandwidth were all these parameters are fine: for example, between 8 and 17 GHz.

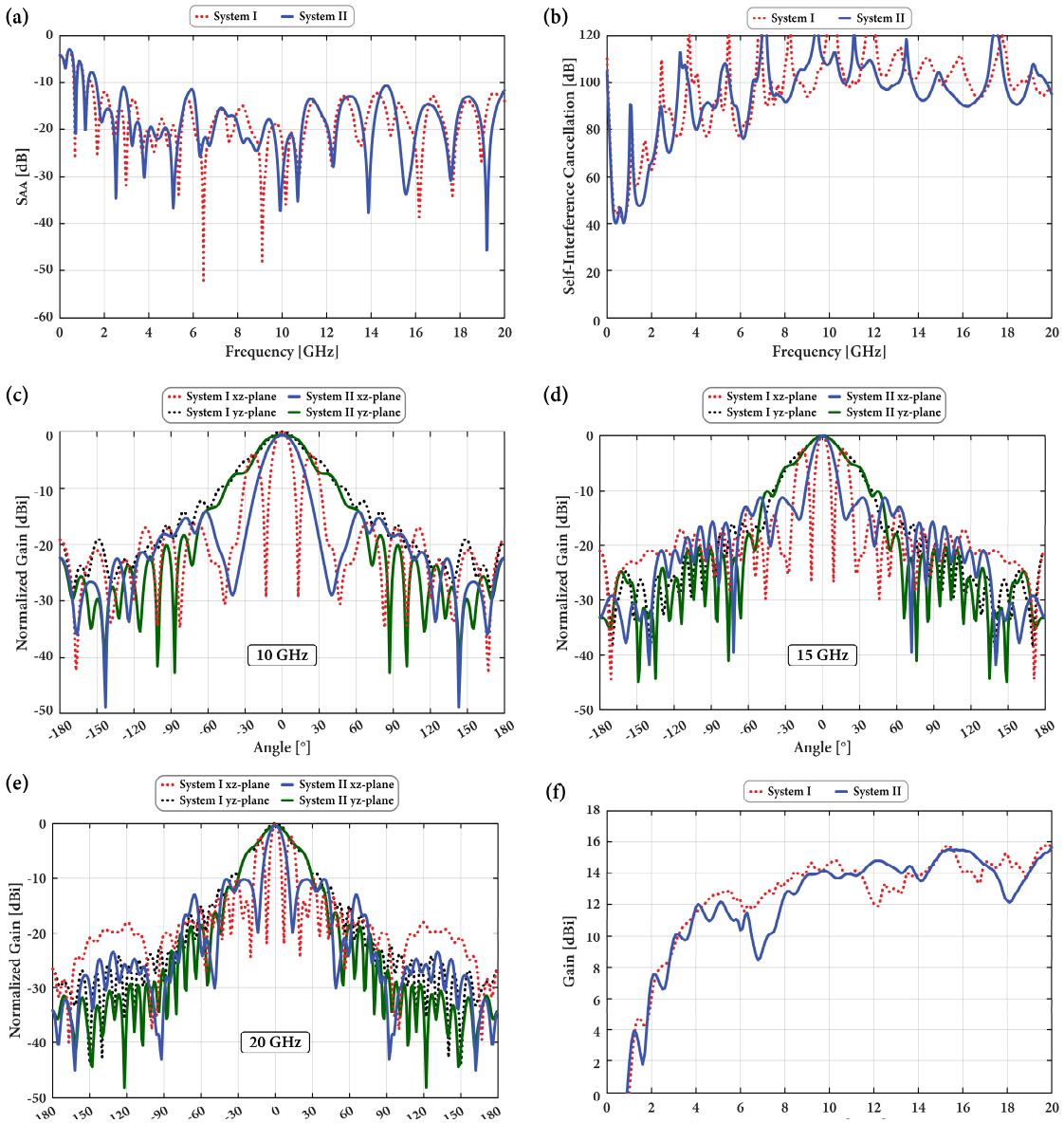

Figure 5: simulated (a) system matching, (b) self-interference cancellation, (c), (d) and (e) radiation pattern plots at 10, 15 and 20 GHz respectively, and (f) system gain.

Finally, System I and System II scored 11.03 and 10.78 in simulation (From Fig. 5), respectively, on the previously mentioned FoM that is dedicated for wideband in-band full-duplex antenna systems. And based on them, it seems that the gain dips do not severely affect the performance of the modified antenna array of System II.

3. Conclusion

In summary, this paper presented an ultra-wideband in-band full-duplex antenna system formed of 3D-printed Vivaldi antennas and two wideband baluns. The system manages to overcome the mechanical defects of a previous work while maintaining an acceptable performance. The fabricated prototype can achieve about 40 to 80 dB of self-interference cancellation in the frequency range from 4.4 GHz to 28.65 GHz, and an average gain of 9.8 dBi with a directive end-fire radiation pattern. It was observed that some grating lobes exist in its radiation pattern alongside the main lobe, and those grating lobes result from the excessive separation distance between the opposite antennas, especially when it exceeds a half-wavelength.

To mitigate grating lobes inherent in such array, the Vivaldi antennas' size was reduced partially at the bottom and the bodies of the antennas were exponentially tapered. In the array, this allows bringing the antennas closer together at their bottom parts, reducing the distance between the radiating slots, which translates to grating lobes reduction especially at higher frequencies. The modified system can achieve, in simulation, a decade matching bandwidth from 2 to 20 GHz with more than 60 dB of self-interference cancellation and 12.8 dBi of average gain. While grating lobes remain at least 10 dB less than the main lobe level throughout the matching bandwidth.

The proposed grating lobes reduction approach appears not to deteriorate system matching and self-interference cancellation performance, but it deepens some gain dips occurring at some frequencies. The gain dips are accompanied by a strong power coupling between the opposite antennas, which is thought to be caused by the profile of the antenna and the size of the matching stubs and their proximity. Several solutions are being investigated for this problem, including but not limited to manipulating the shape and position of the matching stubs, inserting absorbing materials between the antennas, creating corrugations to confine or discharge the direct power coupling. And finally, a prototype of the modified array is sought to be fabricated and measured once the above-mentioned problem is solved.

Finally, it might be beneficial to shield the baluns and isolate them from one another, to prevent any coupling between them and the antennas. Also, it is worth to find a way to integrate the baluns within the array to eliminate the need for cables and connectors, which should further improve the system's efficiency. Moreover, instead of using the array for in-band full-duplex applications, it can be used as a dual-polarized antenna system with enhanced cross-polarization level by feeding both ports of the system with the same input signal. Or the array can be used to generate circularly polarized signals, by feeding the four antennas signals of equal amplitudes and with sequential phase values of 0°, 90°, 180°, 270°, respectively.

Acknowledgements

This project has been supported by the French Directorate General of Armaments (DGA), the European Regional Development Fund (ERDF) of the European Union, the Brittany Region (France), the Departmental Council of Finistère and Brest Métropole as part of the Cyber-SSI project within the framework of the Brittany State-Region Contract (CPER).

A preliminary version of this work has been published in ICM 2022 [12].

The authors declare that they have no known competing financial interests or personal relationships that could have appeared to influence the work reported in this paper.

References

Add some references on FD from International Journal of Electronics and Communications

[1] Alves, H., Riihonen, T., and Suraweera, H. A., Full-Duplex Communications for Future Wireless Networks. Springer, 2020.

[2] Bharadia, D., McMilin, E., and Katti, S., Full duplex radios. In Proceedings of the ACM SIGCOMM 2013 conference on SIGCOMM, (2013): 375-386.

[3] Kolodziej, K. E., Perry, B. T., & Herd, J. S. (2019). In-band full-duplex technology: Techniques and systems survey. IEEE Transactions on Microwave Theory and Techniques, 67(7), 3025-3041.

[4] Elmansouri, M., Valaleprasannakumar, P., Tianang, E., Etellisi, E., & Filipovic, D. (2017, July). Single and dual-polarized wideband simultaneous transmit and receive antenna system. In 2017 IEEE International Symposium on Antennas and Propagation & USNC/URSI National Radio Science Meeting (pp. 1105-1106). IEEE.

[5] E. A. Etellisi, "Wideband Monostatic Co-Channel Simultaneous Transmit and Receive (C-STAR) Antenna and Array Systems." PhD diss., University of Colorado at Boulder, 2018.

[6] P. V. Prasannakumar, "Wideband bi-static and monostatic STAR antenna systems." PhD diss., University of Colorado at Boulder, 2019.

[7] H. Hijazi, M. Le Roy, R. Lababidi, D. Le Jeune, and A. Pérennec, "Ultra ‐ Wideband Antenna System for In ‐ Band Full ‐ Duplex Applications." IET Microwaves, Antennas & Propagation 15, no. 15, pp. 1853-1865, 2021

[8] H. Hijazi, M. Le Roy, R. Lababidi, D. Le Jeune, and A. Pérennec, "4-40 GHz In-Phase/180 Out-of-Phase Power Dividers with Enhanced Isolation." In 2020 14th European Conference on Antennas and Propagation (EuCAP), pp. 1-5. IEEE, 2020

[9] Veidt, B., Burgess, T., Yeung, K., Claude, S., Wevers, I., Halman, M., Niranjanan, P., Yao, C., Jew, A., and Willis, A. G., Noise performance of a phased-array feed composed of thick Vivaldi elements with embedded low-noise amplifiers. In *2015 9th European Conference on Antennas and Propagation (EuCAP)*, (2015): 1-4, IEEE.

[10] Balanis, C. A., *Antenna Theory: Analysis and Design*. John wiley & sons, 2015.

[11] Chan, K. K. M., Tan, A. E. C., and Rambabu, K., Decade bandwidth circularly polarized antenna array. IEEE Transactions on Antennas and Propagation 61, no. 11 (2013): 5435-5443.

[12] Hijazi, Hadi, Marc Le Roy, Raafat Lababidi, Denis Le Jeune, and Andre Pérennec. "3D-Printed Ultra-Wideband In-Band Full-Duplex Antenna System With Grating Lobes Reduction." In 2022 International Conference on Microelectronics (ICM), pp. 86-89. IEEE, 2022.